SKI Report 91:18

The CALIBRE Source-Term Code:

Technical Documentation for Project -90

P. Robinson
K. Worgan

March 1992

ISSN 1104–1374
ISRN SKI-R-91/18SE

SKI

The CALIBRE Source-Term Code:
Technical Documentation for Project-90

P. Robinson - K. Worgan

SKI TR 91:18

Intera Enviromental Division
Chiltern House
45 Station Road
Henley-on-Thames
Oxfordshire RG9 1AT
UK

March 1992

gotab 96244. Stockholm 1992

SKI-TR 91:18
Version 3

The CALIBRE Source-Term Code: Technical Documentation for Project-90

P. Robinson

K. Worgan

March 1992

Intera Environmental Division
Chiltern House, 45 Station Road, Henley-on-Thames, Oxfordshire RG9 1AT, UK
Tel (0491) 410474 Fax (0491) 576916

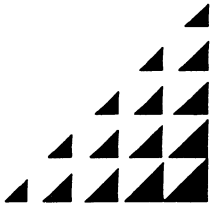

INTERA

The CALIBRE Source Term Code

Summary

A numerical model has been developed which simulates the diffusion of radionuclides from a high-level waste canister, through a backfill region and into a fractured rock matrix. The model includes chain decay and ingrowth, linear equilibrium sorption, solubility limiting and response to a redox front as it emerges from the canister and migrates through the near-field. Radial advection (which approximates the advection downstream from the canister and buffer) is applied in the fracture, in addition to diffusion or dispersion.

This document describes the mathematical model and numerical methods used in developing CALIBRE, together with a number of verification tests which compare the results with those computed using analytic solutions.

Contents

List of Tables

List of Figures

1 Introduction

The CALIBRE computer program has been developed as a modelling tool for the Swedish Nuclear Power Inspectorate's Project-90 reference repository assessment for the disposal of spent nuclear fuel [1]. The conceptual model geometry for CALIBRE is illustrated in figure 1.1, based on the KBS-3 disposal concept. The model itself does not include the buffer material vertically above the canister, nor the emplacement tunnel. The model calculates the behaviour of radionuclides released to the near-field environment after the degradation of a high-level waste canister. Processes modelled include leaching of the nuclides from the solid waste matrix, diffusion through a bentonite backfill surrounding the canister, diffusion through a fractured rock matrix and advection and diffusion in the fracture water. As well as decay and ingrowth of chains of radionuclides, the model includes linear equilibrium sorption and solubility limiting under reducing and oxidising conditions, as it monitors the movement of a redox front which originates in the canister and migrates through the near-field. The redox front information is provided from a stand alone section of the code, which is described elsewhere [2], [3].

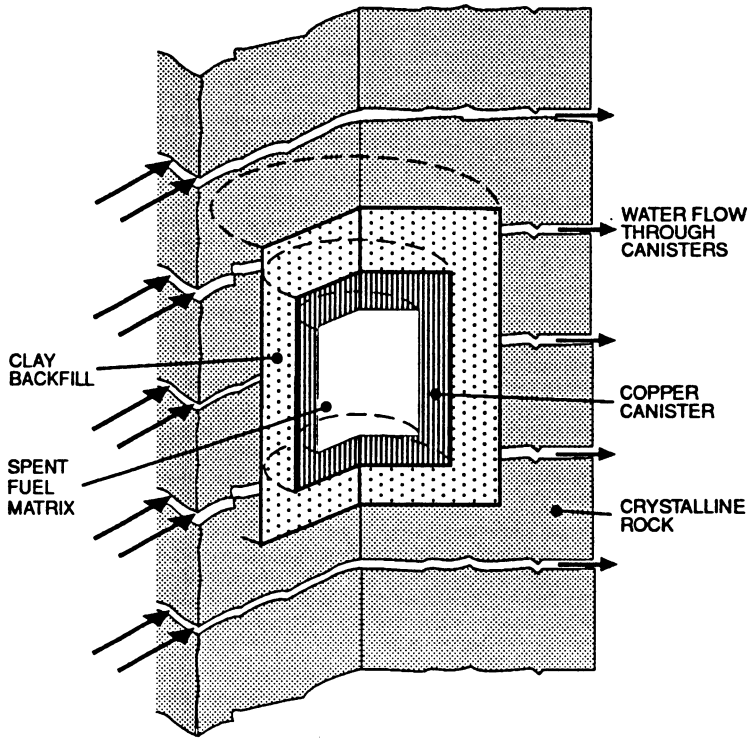

Figure 1.1 The Conceptual Model Geometry in CALIBRE

The mathematical model of radionuclide transport in the near-field is set out in section 2. The original detailed mathematical description of the system is given in the specification document [4] and is not repeated here.

The numerical methods used to solve the equations are described in sections 3-5. This includes the finite difference space discretization and time stepping scheme employed, together with the approach used to handle the advection, diffusion, decay and solubility limiting processes.

Section 6 describes a number of verification problems, where we compare the CALIBRE results with those computed using analytic methods. A detailed description of these methods is given in reference [5]. They show good agreement overall and also indicate areas where care should be taken in using the model, to ensure the accuracy of the results.

2 Mathematical Model

2.1 Transport in the Buffer and Rock Matrix

In the specification document [4] the equations for the release of radionuclides from the canister and their migration through the bentonite and rock matrix were set out. These have been followed with few modifications. The main change is in the canister itself, where axial diffusion is included explicitly. This allows for spatial variation in the total concentrations (that is, sorbed, dissolved in the pore water and precipitated) in the canister, rather than implicity assuming that diffusion results in complete mixing.

In the canister, the main quantities to be solved for are $W_{ij}^C(t)$, the amount of solid waste per unit volume of canister, and $A_{ij}^C(t)$, the total concentration of released nuclides. Suffix ij denotes isotope i of element j . The governing equation for solid waste concentration $W_{ij}^C(t)$ is

$$\frac{dW_{ij}^C(t)}{dt} = -\lambda_{ij} W_{ij}^C(t) + \lambda_{IJ} W_{IJ}^C(t) - k_{ij} W_{ij}^C(t), \tag{1}$$

where λ_{ij} is the decay constant for isotope i of element j, λ_{IJ} is the decay constant for its parent nuclide, and k_{ij} is the fraction released from the solid fuel per year. The release fraction may be constant or time-dependent. Details of the various fuel release models employed in CALIBRE are given in the Project-90 report on the near-field calculations [6].

The total concentration of released isotope i, $A_{ij}^C(t)$ is partitioned into the concentration dissolved in the pore water, $C_{ij}^C(t)$, the concentration sorbed on solid material, $S_{ij}^C(t)$ and the concentration precipitated, $P_{ij}^C(t)$:

$$A_{ij}^C(t) = \varepsilon^C C_{ij}^C(t) + S_{ij}^C(t) + P_{ij}^C(t), \tag{2}$$

where ε^C is the porosity in the canister.

Once released from the solid waste form the nuclides in the pore water diffuse radially into the bentonite, and axially within the degraded canister region. The governing equation for $A_{ij}^C(t)$ is given by

$$\frac{\partial A_{ij}^C(r,z,t)}{\partial t} = -\lambda_{ij} A_{ij}^C(r,z,t) + \lambda_{IJ} A_{IJ}^C(r,z,t) + k_{ij} W_{ij}^C(z,t) + D^B \left[\frac{1}{r}\frac{\partial}{\partial r}\left(r\frac{\partial C_{ij}^C}{\partial r}(r,z,t)\right)\right] + D^C \frac{\partial^2 C_{ij}^C}{\partial z^2}(r,z,t), \tag{3}$$

where D^B the effective pore water diffusion coefficient in the bentonite (assumed valid for the degraded canister/ bentonite region) and D^C is the effective diffusion coefficient in the axial direction in the canister.

The partitioning between dissolved, sorbed and precipitated concentrations in the absence of solubility limits is given by:

$$C^C_{ij}(t) = A^C_{ij}(t)/\alpha^C_j, \quad (4)$$

$$S^C_{ij}(t) = \rho^C K^C_j C^C_{ij}(t), \quad (5)$$

$$P^C_{ij}(t) = 0, \quad (6)$$

where ρ^C is the density of material in the source region, K^C_j is the element-dependent distribution coefficient and α^C_j is the capacity factor given by:

$$\alpha^C_j = \varepsilon^C + \rho^C K^C_j. \quad (7)$$

If at any time the solubility limit for element j, $C^C_j(\mathrm{sol})$ is exceeded inside the container then equation 4 ceases to hold. Instead the dissolved concentration of each isotope is proportional to the ratio of the total isotope concentration to total element concentration:

$$C^C_{ij}(t) = C^C_j(\mathrm{sol})\frac{A^C_{ij}(t)}{\sum_i A^C_{ij}(t)}, \quad (8)$$

where the summation over isotopes includes the stable species. The expression for the sorbed concentration equation 5 is unchanged whilst the precipitate concentration is given by:

$$P^C_{ij}(t) = A^C_{ij}(t) - \alpha^C_j C^C_{ij}(t). \quad (9)$$

Before the canister fails due to corrosion the inventory is calculated using the Bateman equations, and the concentrations released in all states are set to zero. After canister failure, nuclides may be released under reducing conditions in the canister before it becomes fully oxidising.

In the bentonite and rock the governing equations for the A_{ij} are similar to equation 3, except there is no input from a solid waste source. In the bentonite equation 3 becomes:

$$V\frac{\partial A^B_{ij}(r,z,t)}{\partial t} = -\lambda_{ij}A^B_{ij}(r,z,t) + \lambda_{IJ}A^B_{IJ}(r,z,t)$$

$$+ D^B \left[\frac{1}{r} \frac{\partial}{\partial r} \left(r \frac{\partial C_{ij}^B(r,z,t)}{\partial r} \right) + \frac{\partial^2 C_{ij}^B(r,z,t)}{\partial z^2} \right], \quad (10)$$

and in the rock

$$\frac{\partial A_{ij}^R(r,z,t)}{\partial t} = -\lambda_{ij} A_{ij}^R(r,z,t) + \lambda_{IJ} A_{IJ}^R(r,z,t)$$

$$+ D^R \left[\frac{1}{r} \frac{\partial}{\partial r} \left(r \frac{\partial C_{ij}^R(r,z,t)}{\partial r} \right) + \frac{\partial^2 C_{ij}^R(r,z,t)}{\partial z^2} \right], \quad (11)$$

where D^B, D^R are the effective pore water diffusion coefficients in the bentonite and rock respectively. The boundary conditions are as follows:

$$-D^B \frac{\partial C_{ij}^B(r,z,t)}{\partial r}\bigg|_{r=r_1} = F_{ij}^C(t), \quad (12)$$

where r_1 is the canister radius and $F_{ij}^C(t)$ is the radial flux per unit cross-sectional area from the canister into the bentonite:

$$\frac{\partial C_{ij}^B(r,z,t)}{\partial z}\bigg|_{z=0} = \frac{\partial C_{ij}^B(r,z,t)}{\partial z}\bigg|_{z=Z} = 0, \quad (13)$$

where Z is half the axial distance between fractures;

$$C_{ij}^B(r,z,t)\Big|_{\substack{r=r_2 \\ b<z<Z}} = C_{ij}^R(r,z,t)\Big|_{\substack{r=r_2 \\ b<z<Z}}, \quad (14)$$

where r_2 is the radial distance of the bentonite/rock interface from the centre of the canister, and b is fracture half-width;

$$-D^B \frac{\partial C_{ij}^B(r,z,t)}{\partial r}\bigg|_{\substack{r=r_2 \\ b<z<Z}} = -D^R \frac{\partial C_{ij}^R(r,z,t)}{\partial r}\bigg|_{\substack{r=r_2 \\ b<z<Z}}, \quad (15)$$

$$-D^B \frac{\partial C_{ij}^B(r,z,t)}{\partial r}\bigg|_{\substack{r=r_2 \\ 0<z<b}} = -D^R \frac{\partial C_{ij}^R(r,z,t)}{\partial r}\bigg|_{\substack{r=r_2 \\ 0<z<b}}, \quad (16)$$

$$\frac{\partial C_{ij}^R(r,z,t)}{\partial z}\bigg|_{z=Z} = 0, \quad (17)$$

$$-D^R F_s \frac{\partial C_{ij}^R(r,z,t)}{\partial z}\bigg|_{z=b} = -D^F F_s \frac{\partial C_{ij}^F(r,z,t)}{\partial z}\bigg|_{z=b}, \quad (18)$$

where F_s is the fraction of the fracture surface area available for matrix diffusion. This may be less than one, to account for channelling in the fractures. The far boundary condition is given by

$$C_{ij}^R(r,z,t)\Big|_{r\to\infty} = 0. \tag{19}$$

In the program, the boundary condition 19 is replaced by

$$C_{ij}^R(r,z,t)\Big|_{r=r_3} = 0, \tag{20}$$

where r_3 is chosen to be far enough away from the canister for the condition to be true.

Partitioning between dissolved, sorbed and precipitated states in each material is treated in the same manner as in the canister (equations 4 - 9) with appropriate choice of the material-dependent quantities of density, porosity and distribution coefficients.

2.2 Transport in the Fracture

The mass transfer in the fracture can be described in terms of the continuity equation for the total concentration A of radionuclides, comprising the fractions dissolved in the water, sorbed on the fracture walls and precipitated:

$$\begin{aligned}\frac{\partial A_{ij}(t)}{\partial t} &= -\lambda_{ij}A_{ij}(t) + \lambda_{IJ}A_{IJ}(t) \\ &\quad + D^W\left[\frac{1}{r}\frac{\partial}{\partial r}\left(r\frac{\partial C_{ij}}{\partial r}\right) + \frac{\partial^2 C_{ij}}{\partial z^2} + \frac{1}{r^2}\frac{\partial^2 C_{ij}}{\partial \theta^2}\right] \\ &\quad + v_r\frac{\partial C_{ij}}{\partial r} + v_\theta\frac{1}{r}\frac{\partial C_{ij}}{\partial \theta}\end{aligned} \tag{21}$$

The subscript ij denotes isotope i of element j, with IJ representing the parent nuclide. A is the total concentration of the nuclide, C is the concentration dissolved in the water, D^W is the diffusion coefficient of free water, v_r and v_θ are the radial and tangential components of the flow velocity and λ_{ij}, λ_{IJ} are the decay constants of the nuclide and its parent.

The partitioning between dissolved, sorbed and precipitated concentrations in the absence of solubility limits is given by:

$$C_{ij}(t) = \frac{A_{ij}(t)}{\alpha_j} \tag{22}$$

$$S_{ij}(t) = \rho^R K_j^R (1-\epsilon^R)\frac{\delta a}{\theta} C_{ij}(t) \quad (23)$$

$$P_{ij}(t) = 0 \quad (24)$$

where ρ^R, K_j^R, ϵ^R are the density, distribution coefficient (of element j) and porosity of the rock, θ is the fractured rock porosity, δ is the effective depth of surface sorption on the fracture walls and a is the channelling parameter, or specific wet surface area per unit volume of fractured rock. This definition corresponds with that used in the Project-90 geosphere transport code, CRYSTAL [7]. The capacity factor α_j of the fracture is given by:

$$\alpha_j = 1 + \rho^R K_j^R (1-\epsilon^R)\frac{\delta a}{\theta}, \quad (25)$$

where the porosity of the fracture is 1. Unlike the CRYSTAL code, where surface sorption is set to zero if matrix diffusion is modelled, surface sorption is always accounted for in CALIBRE. This is required owing to the space discretization approach used to solve the model equations. The fracture and its interface with the rock is represented by a single layer of cells, each comprising both rock and fracture. Surface sorption is therefore included to account for the sorption which occurs in the rock portions of these cells.

If the solubility limit $C_j(sol)$ of element j is exceeded in the fracture then the dissolved concentration of each isotope is proportional to the ratio of the total isotope concentration to the total element concentration:

$$C_{ij}(t) = C_j(sol)\frac{A_{ij}(t)}{\sum_i A_{ij}(t)} \quad (26)$$

where the summation over isotopes includes the stable species. The expression for the sorbed concentration (23) is unchanged whilst the precipitate concentration is given by:

$$P_{ij}(t) = A_{ij}(t) - \alpha_j C_{ij}(t) \quad (27)$$

The boundary conditions at the edges of the fracture are now given by:

$$\left.\frac{\partial C}{\partial z}^F\right|_{z=0} = 0 \quad (28)$$

$$\left.-D^R F_s \frac{\partial C}{\partial z}^R\right|_{z=b} = \left.-D^F F_s \frac{\partial C}{\partial z}^F\right|_{z=b} \quad (29)$$

$$\left.-D^B \frac{\partial C}{\partial r}^B\right|_{r=r_2} = \left.-D^F \frac{\partial C}{\partial r}^F\right|_{r=r_2} \quad (30)$$

The boundary condition (28) represents the zero flux requirement at the midpoint of the fracture. Boundary conditions (29) and (30) represent the flux continuity requirements at the rock-fracture and bentonite-fracture interfaces, respectively. The superscripts R, B and F denote the rock, bentonite and fracture respectively, r_2 is the radius of the bentonite-rock interface and b is the fracture half-width. F_s is the fraction of the surface area available for matrix diffusion. It corresponds to the channelling parameter a employed here (in equations 23, 25 above) and in the CRYSTAL code. For parallel plate fractures with spacing S between fractures and surface area A_s, a and F_s are related in the following manner, according to the definition of a as the fracture wall surface area available for matrix diffusion per unit volume of fractured rock:

$$a = \frac{2F_sA_s}{A_sS}, \tag{31}$$

which gives

$$a = \frac{2F_s}{S}. \tag{32}$$

A further condition of zero concentration is imposed at a radius r_3 sufficiently far from the fracture edge so that it does not influence the flux into the fracture. This radius also defines the far radial boundary of the discretized mesh.

The radial and tangential flow velocity components v_r, v_θ may be derived from the solution to Laplace's equation for potential flow around a cylinder. They may be written in the form:

$$v_r = v\cos\theta\left(1 - \frac{{r_2}^2}{r^2}\right) \tag{33}$$

$$v_\theta = -v\sin\theta\left(1 + \frac{{r_2}^2}{r^2}\right) \tag{34}$$

where v is the velocity far from the cylinder. The flow field is illustrated schematically in figure 2.1.

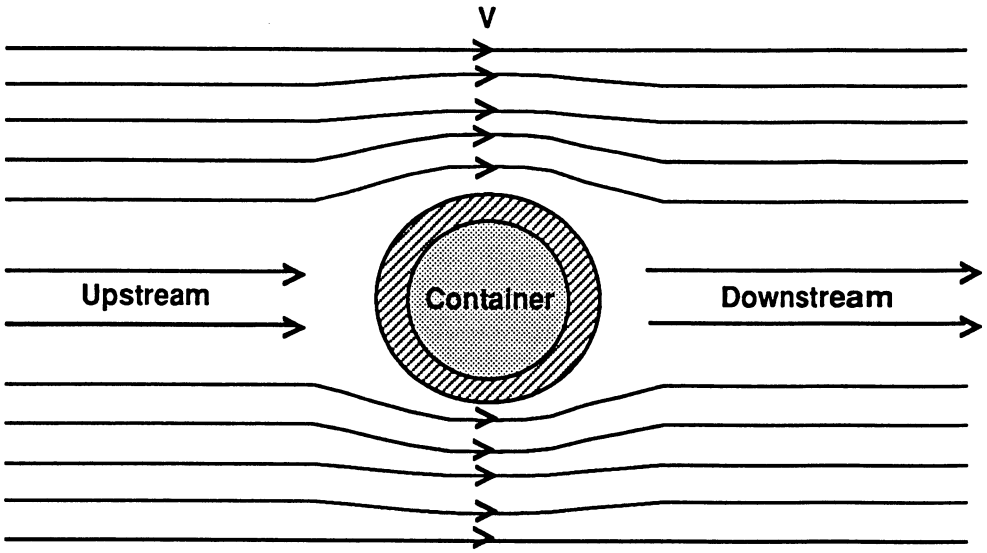

Figure 2.1 Schematic Representation of the Flow Field Around a Cylindrical Container in the Fracture Plane

The flow around the canister and bentonite destroys the cylindrical symmetry of the system, resulting in the three-dimensional mass transfer equation (21). Figure 2.2 illustrates the radial and angular dependence of the contaminants in the cells of the discretized region in the fracture plane. To avoid the complication and computational cost of a fully three-dimensional model, an approximation to the flow has been derived which accounts for the net advective mass transfer downstream from the canister, within a two-dimensional model.

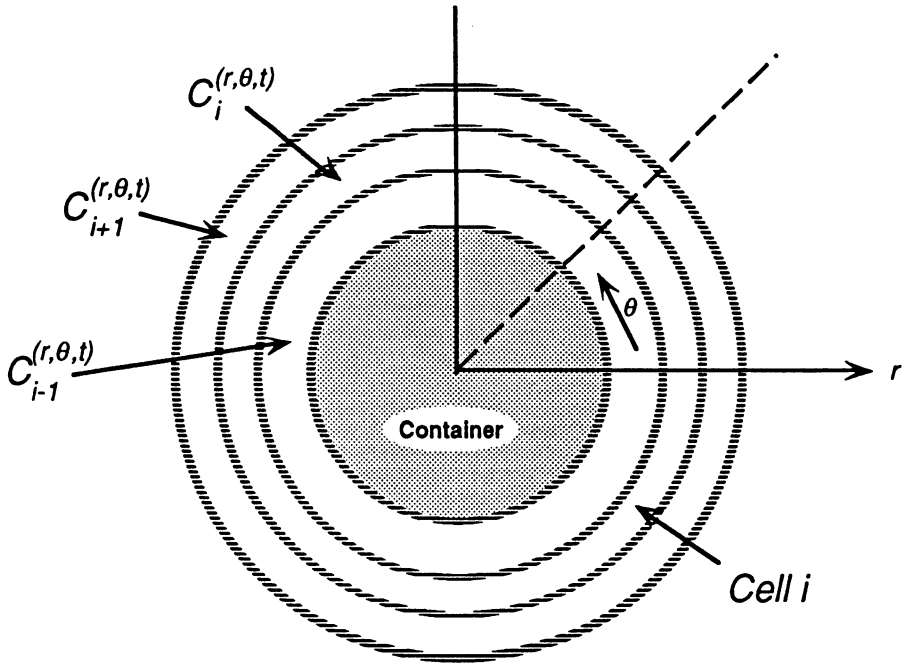

Figure 2.2 Cell Discretization in the Fracture Plane, Showing Radial and Angular Dependence of Contaminant Concentration

In the approximation, the angular dependence of the dissolved concentration is assigned to a weighting function, $f(\theta)$:

$$C(r,\theta) = C(r)f(\theta) \tag{35}$$

where $C(r)$ is the average concentration in the fracture water at radius r. For very thin fractures it is also assumed that there is no vertical variation in dissolved concentration within the fracture. The average concentration $C(r)$ is obtained by averaging $C(r,\theta)$ over θ:

$$C(r) = \frac{1}{2\pi}\int_0^{2\pi} C(r,\theta)d\theta \tag{36}$$

This implies that the weighting function $f(\theta)$ must satisfy the condition:

$$\frac{1}{2\pi}\int_0^{2\pi} f(\theta)d\theta = 1 \tag{37}$$

The continuity equation (21) may also be expressed in terms of the diffusive and advective flux components:

$$\frac{\partial A_{ij}(t)}{\partial t} = -\lambda_{ij}A_{ij}(t) + \lambda_{IJ}A_{IJ}(t) - \frac{1}{r}\frac{\partial}{\partial r}(rJ_r) - \frac{\partial J_z}{\partial z} - \frac{1}{r}\frac{\partial J_\theta}{\partial \theta} - \frac{\partial J_r^a}{\partial r} - \frac{1}{r}\frac{\partial J_\theta^a}{\partial \theta}, \quad (38)$$

where the diffusive flux terms are given by:

$$J_r = -D^W\frac{\partial C_{ij}}{\partial r}, \quad (39)$$

$$J_\theta = -\frac{D^W}{r}\frac{\partial C_{ij}}{\partial \theta}, \quad (40)$$

$$J_z = -D^W\frac{\partial Cij}{\partial z}, \quad (41)$$

and the advective flux terms are given by:

$$J_r^a = -v_r C_{ij}, \quad (42)$$

$$J_\theta^a = -v_\theta C_{ij}. \quad (43)$$

Substituting the weighting function approximation into the angular-dependent flux terms gives:

$$J_\theta = -\frac{D^W}{r}\frac{C(r)}{2\pi}\left[\int_{\pi/2}^{3\pi/2}\frac{\partial f(\theta)}{\partial \theta}d\theta + \int_{-\pi/2}^{\pi/2}\frac{\partial f(\theta)}{\partial \theta}d\theta\right] \quad (44)$$

$$J_r^a = -v\left(1-\frac{r_2^2}{r^2}\right)\frac{C(r)}{2\pi}\left[\int_{\pi/2}^{3\pi/2} f(\theta)\cos\theta d\theta + \int_{-\pi/2}^{\pi/2}\cos\theta f(\theta)d\theta\right] \quad (45)$$

$$J_\theta^a = v\left(1+\frac{r_2^2}{r^2}\right)\frac{C(r)}{2\pi}\left[\int_{\pi/2}^{3\pi/2} f(\theta)\sin\theta d\theta + \int_{-\pi/2}^{\pi/2} f(\theta)\sin\theta d\theta\right], \quad (46)$$

where we have split the weighting function into an upstream term for θ ranging from $\pi/2$ to $3\pi/2$ and a downstream term for θ ranging from $-\pi/2$ to $\pi/2$.

If $f(\theta) = 1$ for all θ, then all the above terms are zero. Non-trivial choices for the weighting function, for which J_r^a is non-zero and J_θ and J_θ^a are zero include:

- $f(\theta) = 2$ on the downstream side and zero on the upstream side,
- $f(\theta) = \pi\cos\theta$ on the downstream side and zero on the upstream side.

The radial flux term may be written:

$$J_r^a = v\left(1 - \frac{r_2^2}{r^2}\right)(\beta_0 - \beta_1)\,C(r), \tag{47}$$

where

$$\beta_0 = -\frac{1}{2\pi}\int_{\pi/2}^{3\pi/2} \cos\theta f(\theta) d\theta \tag{48}$$

and

$$\beta_1 = \frac{1}{2\pi}\int_{-\pi/2}^{\pi/2} \cos\theta f(\theta) d\theta \tag{49}$$

Hence, for $f(\theta) = 2$, $\beta_0 = 0$ and $\beta_1 = 2/\pi$, and for $f(\theta) = \pi\cos\theta$, $\beta_0 = 0$ and $\beta_1 = \pi/4$.

The radial flow and downstream weighted concentration approximation are illustrated schematically in figure 2.3.

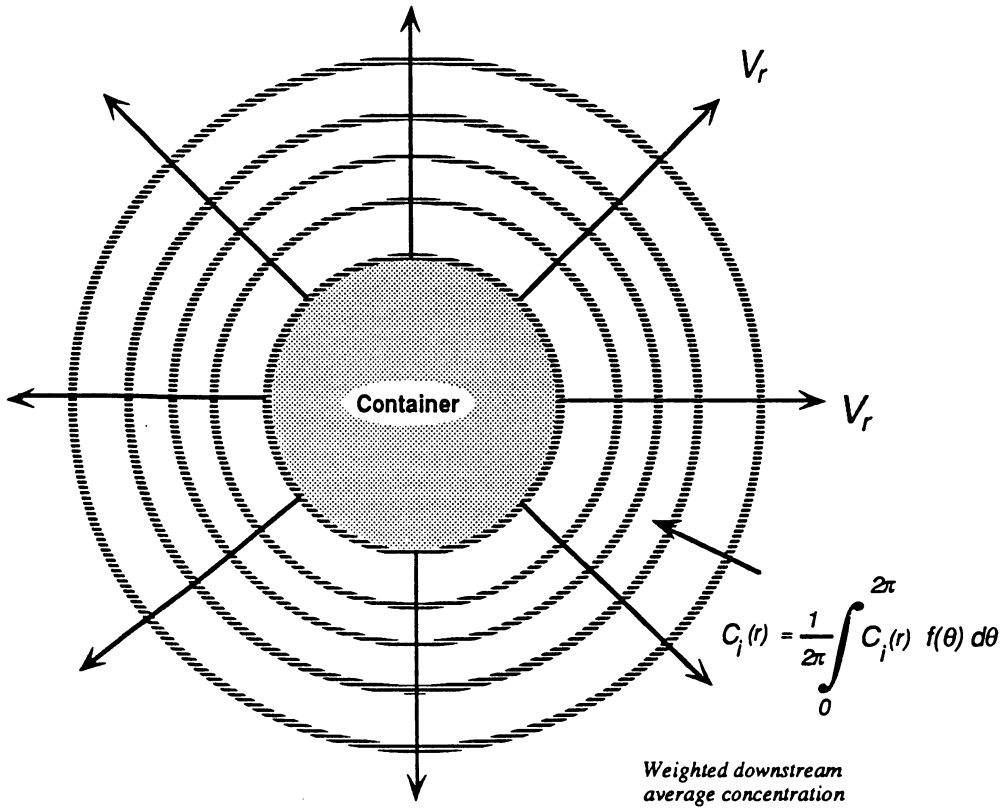

Figure 2.3 Radial Concentration and Flow Approximation

2.3 Precipitate Formation and Dissolution

In CALIBRE, the independent variable solved for is the total concentration $A_{ij}(t)$, where the subscript refers to isotope i of element j. The total

concentration is partitioned into the concentration dissolved in the pore water, $C_{ij}(t)$, the concentration sorbed on solid material, $S_{ij}(t)$ and the concentration precipitated, $P_{ij}(t)$:

$$\begin{aligned} A_{ij}(t) &= \epsilon C_{ij}(t) + S_{ij}(t) + P_{ij}(t) \\ &= \epsilon C_{ij}(t) + \rho K_j C_{ij}(t) + P_{ij}(t) \\ &= \alpha_j C_{ij}(t) + P_{ij}(t) \end{aligned} \tag{50}$$

where ϵ is the porosity of the material (bentonite, rock or fracture), ρ is the material density, K_j is the distribution or sorption coefficient of element j, and α_j is the capacity factor.

If the precipitate is zero, then the dissolved concentration is related to the total concentration via the capacity factor:

$$C_{ij}(t) = A_{ij}(t)/\alpha_j. \tag{51}$$

If the solubility limit $C_j(sol)$ is exceeded, then the dissolved concentration of each isotope is proportional to the ratio of the total isotope concentration to the total element concentration:

$$\begin{aligned} C_{ij}(t) &= C_j(sol)\frac{A_{ij}(t)}{\Sigma_i A_{ij}(t)} \\ &= A_{ij}(t)/\alpha' \end{aligned} \tag{52}$$

where α' is an 'effective' capacity factor, which varies according to the extent to which the solubility limit is exceeded.

The precipitate concentrations in each cell are accounted for explicitly wherever they arise. If the solubility limit changes at any time, then for cases with precipitate concentrations which exceed the dissolved concentration, the precipitate is released at a constant fractional release rate which is element dependent and user-defined. Once the precipitate concentration falls below the dissolved concentration, the remainder is released into solution in one time-step, and the precipitate concentration set to zero. The release fractions used in Project-90 are similar to those calculated for release from the solid fuel matrix. This technique is employed to maintain the accuracy of the calculations, which may be upset if relatively large amounts of precipitate are released into solution in a single time-step. It may also be argued on physical grounds that dissolution of precipitate is not normally instantaneous, and is more probably controlled by diffusion and/or surface effects. Another reason for releasing precipitate slowly is that the redox front itself migrates slowly in space and time, rather than in the discrete steps imposed by the numerical model.

3 Numerical Methods

The basic approach to solving the equations used within CALIBRE involves a finite difference discretization in the spatial dimensions with a time-stepping scheme to handle the time dimension. Within each time step the radioactive decay and ingrowth part of the system is decoupled from the diffusion part. The solubility limits are used to derive relationships between concentration in the pore water and total concentration, which is held fixed for the duration of each time-step. With these approximations, the diffusion for each radionuclide is calculated separately. An alternating direction implicit (ADI) scheme is used, allowing reasonable time-steps in most cases, with good accuracy. All these aspects of the method are expanded in the following sections.

3.1 Spatial Discretization

The spatial discretization used is based on a rectangular array of cells in r-z co-ordinates. Figure 3.1 shows how these cells fit into the physical structure of canister, bentonite, rock and fracture. Each cell has a node whose position is used when gradient calculations are made. Where irregular cell sizes are used the cell boundaries are placed symmetrically between nodes. If the cells are all of the same size then the nodes are at the cell centres. Figure 3.1 shows a rather coarse grid for clarity; in practice the grid would be much finer.

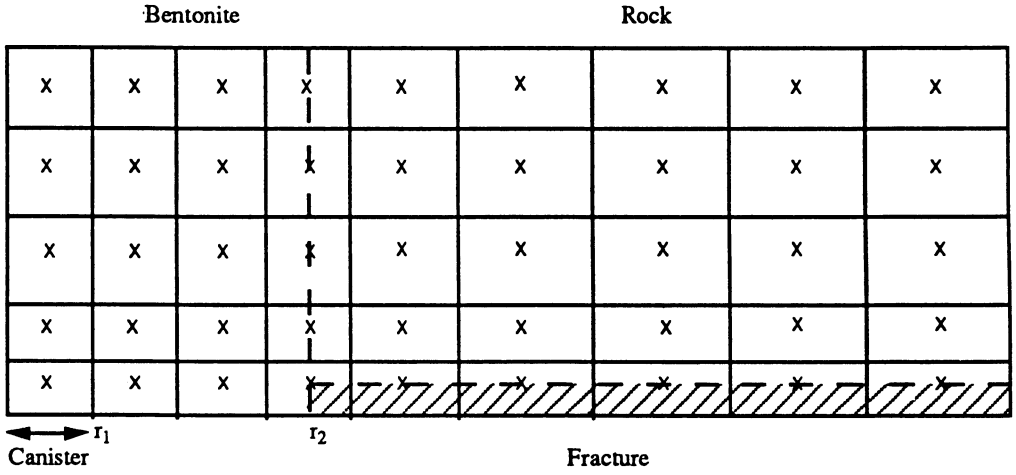

Figure 3.1 Schematic Representation of Spatial Discretization

The independent variable solved for is the average amount per unit volume within each cell. This is related to the pure-water concentration through the capacity factor α, and where relevant the solubility limit. In either

case we can denote the ratio of amount per unit volume to pore-water concentration by an effective capacity factor α', which is time dependent because of the solubility limits and because of the presence of a moving redox front. The movement of radionuclides between cells is determined by the diffusive terms in the equations.

We label the columns by i and the rows by j and then the discrete version of the basic equation 10 or 11 for cell ij in the bentonite or rock is

$$\begin{aligned} V_{ij}\frac{dA_{ij}(t)}{dt} = \quad & D_{i-\frac{1}{2},j}S_{i-\frac{1}{2},j}\frac{C_{(i-1),j}-C_{i,j}}{r_i-r_{(i-1)}} \\ & +D_{i+\frac{1}{2},j}S_{i+\frac{1}{2},j}\frac{C_{(i+1),j}-C_{i,j}}{r_{(i+1)}-r_i} \\ & +D_{i,j+\frac{1}{2}}S_{i,j+\frac{1}{2}}\frac{C_{i,(j+1)}-C_{i,j}}{z_{j+1}-z_j} \\ & +D_{i,j-\frac{1}{2}}S_{i,j-\frac{1}{2}}\frac{C_{i,(j-1)}-C_{i,j}}{z_j-z_{j-1}} \\ & -\lambda V_{ij}A_{ij}+\lambda_p V_{ij}A^p_{ij}. \end{aligned} \tag{53}$$

where the subscript and superscript p indicates the parent nuclide, and

V_{ij} - volume of cell i,j

A_{ij} - average total concentration in cell i,j

r_i - radial co-ordinate for cell-nodes in column i

z_j - axial co-ordinate for all nodes in row j

C_{ij} - average pore-water concentration in cell i,j $\quad(A_{ij}/\alpha'_{ij})$

$D_{i-\frac{1}{2},j}$ diffusion coefficient on the boundary between cells $i-1,j$ & i,j

$D_{i+\frac{1}{2},j}$ diffusion coefficient on the boundary between cells i,j & $(i+1),j$

$D_{i,j+\frac{1}{2}}$ diffusion coefficient on the boundary between cells i,j & $i,(j+1)$

$D_{i,j-\frac{1}{2}}$ diffusion coefficient on the boundary between cells $i,(j-1)$ & i,j

$S_{i-\frac{1}{2},j}$ is the surface area between cells $i-1,j$ & $i,j = \frac{\pi(r_{(i-1)}+r_i)\times(z_{(j+1)}-z_{(j-1)})}{2}$

$S_{i+\frac{1}{2},j}$ is the surface area between cells $i,\ j$ & $i+1,\ j = \frac{\pi(r_{(i+1)}+r_i)\times(z_{(j+1)}-z_{(j-1)})}{2}$

$S_{i,j+\frac{1}{2}}$ is the surface area between cells $i,\ j$ & $i,\ j+1 = \frac{\pi[r^2_{(i+1)}+\ 2r_i(r_{(i+1)}-r_{(i-1)})-r^2_{(i-1)}]}{4}$

$S_{i,j-\frac{1}{2}}$ is the surface area between cells $i,\ j-1$ & $i,\ j = S_{i,j+\frac{1}{2}}$

Transport in the fracture is described by equation 21, which may be discretized in terms of the flux entering and leaving a cell across its bound-

aries. For a cell centred on column i and row j the continuity equation becomes:

$$\begin{aligned}\frac{\partial}{\partial t}(A_{ij}V_{ij}) = & -\lambda V_{ij}A_{ij} + \lambda^p V_{ij}A^p_{ij} \\ & + D^W S_{i-\frac{1}{2},j}\frac{C_{i-1,j}-C_{i,j}}{r_i-r_{i-1}} + D^W S_{i+\frac{1}{2},j}\frac{C_{i+1,j}-C_{i,j}}{r_{i+1}-r_i} \\ & + D^W S_{i,j+\frac{1}{2}}\frac{C_{i,j+1}-C_{i,j}}{z_{j+1}-z_j} + D^W S_{i,j-\frac{1}{2}}\frac{C_{i,j-1}-C_{i,j}}{z_j-z_{j-1}} \\ & + \delta z_j v\frac{r_i+r_{i+1}}{2}\left(1-\frac{4r_2^2}{(r_i+r_{i+1})^2}\right)\{\beta_0 C_{i+1}-\beta_1 C_i\} \\ & - \delta z_j v\frac{r_i+r_{i-1}}{2}\left(1-\frac{4r_2^2}{(r_i+r_{i-1})^2}\right)\{\beta_0 C_i-\beta_1 C_{i-1}\} \qquad (54)\end{aligned}$$

where subscript and superscript p denote the parent nuclide and

V_{ij} is the volume of cell i,j,

C_{ij} is the average dissolved concentration,

r_i is the radial co-ordinate of all cells in column i,

z_j is the vertical co-ordinate for all cells in row j,

δz_j is the depth of all cells in row j,

D^W is the free diffusivity of water,

$S_{i-\frac{1}{2},j} = \pi(r_i + r_{i-1})\delta z_j$ is the surface area between cells $i-1,j$ and i,j,

$S_{i+\frac{1}{2},j} = \pi(r_i + r_{i+1})\delta z_j$ is the surface area between cells i,j and $i+1,j$,

$S_{i,j+\frac{1}{2}} = \frac{\pi}{4}(r_{i+1} - r_{i-1})(r_{i+1} + 2r_i + r_{i-1})$ is the surface area between cells $i,j-1$ and i,j, and

$S_{i,j-\frac{1}{2}} = S_{i,j+\frac{1}{2}}$ is the surface area between cells i,j and $i,j+1$.

If β_0 is chosen to be zero then the approximation for the advective term takes the form of a single-point upstream weighting approximation. i.e. in computing the advective flux across a cell boundary, we take the concentration in the cell from which the contaminants are flowing. Such approximations are often preferred in the solution of difference equations for advective flow, as they help to reduce the propagation of numerical errors.

3.2 Outputs

The main output quantity of interest is the total flux leaving the system at the far boundary. The condition imposed here is one of zero concentration, so the flux $F(t)$ is simply calculated by monitoring the total amounts lost to the end cells over each time-step:

$$F(t) = \sum_{j=1}^{m} V_{ij} \frac{A_{ij}(r = r_3, z_j, t)}{\Delta t}, \tag{55}$$

where the summation is taken over the complete row of cells at the far boundary and Δt is the time-step.

Additional outputs which are calculated include the concentrations and precipitate amounts (if any) at each gridpoint, the flux from the canister to the bentonite and the flux across the bentonite/rock/fracture interface. The latter are defined as follows:

$$F^C(t) = \sum_{j=1}^{m} S_{ij}(r_1) D^c \frac{\Delta C_{ij}(r = r_1, z_j, t)}{\Delta r}, \tag{56}$$

$$F^B(t) = \sum_{j=1}^{m} S_{ij}(r_2) D^c \frac{\Delta C_{ij}(r = r_2, z_j, t)}{\Delta r}, \tag{57}$$

where the S_{ij} are the interface cross-sectional areas and the gradient of the concentration is calculated using a first-order finite difference approximation across neighbouring cells.

3.3 Time Stepping

The discretized equations could be solved by many different time-stepping schemes. There are however a number of characteristics of the current problem which narrow the choice considerably.

Firstly, the moving redox front leads to sudden changes in properties. This rules out time-stepping schemes which use the history of the solution as guidance to the solution at the next time.

The next point to consider is the possibility of diverse timescales. Highly absorbed nuclides will move very slowly, while non-sorbed ones may move rapidly. Some nuclides have very short half-lives while others have very long ones. This suggests that rather short time-steps may be required, which calls for the use of a computationally efficient scheme.

Finally the solubility limitation requires that all isotopes of an element are solved for simultaneously, again pointing to the need for a very efficient scheme.

Combining these considerations, the method we have chosen is based on the alternating direction implicit (ADI) algorithm. This separates the two space dimensions, treating one implicitly and one explicitly for half a timestep and then switching over for the second half. This requires the inversion of nothing worse than tridiagonal matrices.

In the same spirit we separate the calculation of radioactive decay and ingrowth from the diffusion calculation. Also the value of α', the ratio between total and pore water concentrations, is fixed in each cell for the duration of the timestep.

Thus the steps involved in a timestep are

1. Decay and ingrowth for each cell, including the source cells.
2. Calculate α' for each cell, using properties implied by the redox front position halfway through the time-step.
3. Calculate partitioning between dissolved and precipitated species.
4. For each nuclide, apply the ADI diffusion step
   a) implicit in z , explicit in r ,
   b) explicit in z, implicit in r
5. Recalculate the partitioning of dissolved and precipitaed species.

The length of timestep is limited by the explicit parts of the ADI scheme. To avoid instabilities it is recommended that

$$\frac{1}{2}\Delta t < \frac{1}{2}\frac{(\Delta r)^2}{D}\alpha'$$

and

$$\frac{1}{2}\Delta t < \frac{1}{2}\frac{(\Delta z)^2}{D}\alpha'$$

where Δr and Δz are the cell sizes in the two directions.

The timestep calculation is dominated at first by the capacity factors for the relatively non-sorbed nuclides, which are in turn governed by the prevailing chemical conditions. Generally the distribution coefficients are smaller under oxidising conditions, so that once the canister has become fully oxidising, lower values of capacity factors are required. Non-sorbed nuclides diffuse more quickly through the system, however, so that once their concentration is effectively zero, the timestep can be readjusted, provided the relevant nuclides are not daughters which are growing in.

4 Code Verification

The code has been verified where possible against analytic solutions. The analytical model and methods used to solve the equations are described in reference [5]. Basically each of the following tests involve the diffusion of material placed at the inner radial boundary of a thick cylinder. In each case zero-flux conditions are imposed at the inner boundary and upper surface of the thick cylinder, together with a zero concentration condition at the far radial boundary. The lower boundary condition is specified as zero-flux or zero concentration. The latter condition would represent a situation in which advective flow in the fracture is sufficiently fast to maintain an effectively zero concentration of contaminants there.

In the analytical model, a source is introduced at the inner boundary as a line (or surface) source. This may be a pulse or delta function source at time zero, or a source of constant concentration. It may be distributed evenly across the height of the cylinder, or have a z-coordinate dependence. In the numerical model, the line source is approximated by specifying the initial total concentration in each of the innermost cells. i.e. the source is actually dispersed in a thin, cylindrical region.

4.1 One-Dimensional Radial Diffusion with a Delta-Function Source Term

The physical system modelled is shown in figure 4.1. A thick cylinder of inner radius 0.5 (arbitrary) units and outer radius 10 units has zero flux boundary conditions at its inner radius and at the upper and lower surfaces, while the concentration at the outer boundary is fixed at zero. A delta function source of strength 10 units is input at zero time at the inner boundary with zero concentration everywhere else. The cylinder material has a diffusion coefficient of 0.01 arbitrary units (L^2T^{-1}) and a capacity factor of 0.1 (dimensionless).

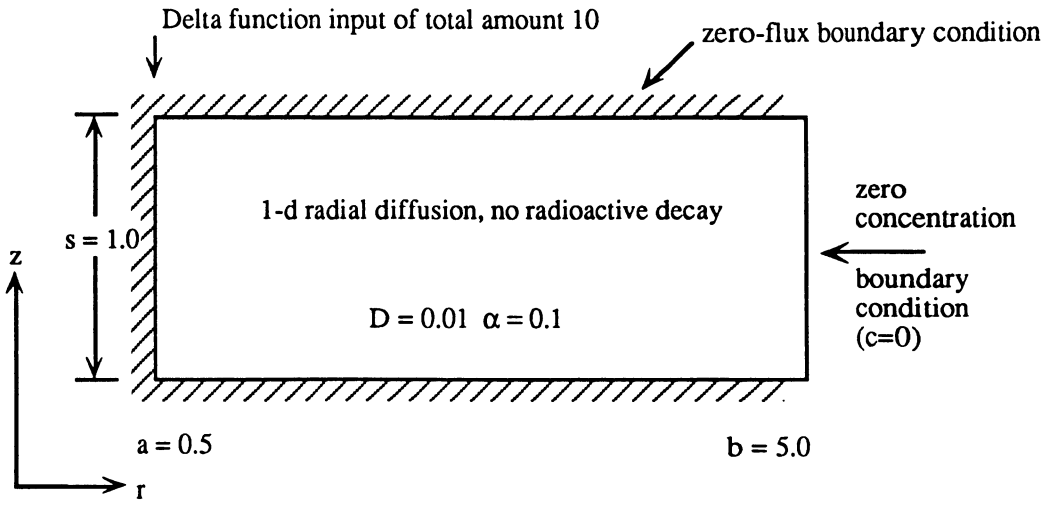

Figure 4.1 Schematic Representation of Test Case 1

The cylindrical region is discretized using a radial grid spacing of 0.2 units, with 22 radial cells in each layer. Vertical grid spacings of 0.2, 0.4 and 0.2 are used, with grid coordinates of 0.1, 0.3, 0.7 and 0.9. The total number of grid cells is 88.

The source is distributed in the first layer of cells with a total concentration in each cell given by $10/V$, where V is the total volume of the innermost cells. A time-step of 20 units is used.

The results for the numerical and analytic models are compared at various output times in table 4.1. At early times, the numerical model results are higher for points beyond a radius of 1.0, and slightly lower in the inner cells. This may be attributed to the source distribution approximation of the delta-function source, together with the dispersion introduced by the finite difference and time-stepping approximations. At later times, excellent agreement is achieved throughout the grid.

Time	Radial Coordinate	Vertical Coordinate	Concentration	
			(Numerical)	(Analytic)
0.5	1.0	0.5	1.40×10^{1}	1.44×10^{1}
	2.0	0.5	8.88×10^{-3}	4.97×10^{-4}
	3.0	0.5	6.76×10^{-7}	-6.93×10^{-8}
	4.0	0.5	2.54×10^{-11}	-6.44×10^{-8}
1.0	1.0	0.5	1.70×10^{-1}	1.75×10^{-1}
	2.0	0.5	1.56×10^{-1}	9.35×10^{-2}
	3.0	0.5	1.16×10^{-4}	3.55×10^{-6}
	4.0	0.5	2.33×10^{-8}	-3.09×10^{-8}
2.0	1.0	0.5	1.49×10^{-1}	1.50×10^{1}
	2.0	0.5	1.07	1.03
	3.0	0.5	1.09×10^{-2}	5.96×10^{-3}
	4.0	0.5	2.63×10^{-5}	2.93×10^{-6}
5.0	1.0	0.5	9.22	9.24
	2.0	0.5	2.99	3.01
	3.0	0.5	3.74×10^{-1}	3.65×10^{-1}
	4.0	0.5	1.94×10^{-2}	1.65×10^{-2}
10.0	1.0	0.5	5.63	5.64
	2.0	0.5	3.14	3.15
	3.0	0.5	1.07	1.07
	4.0	0.5	2.16×10^{-1}	2.19×10^{-1}
20.0	1.0	0.5	3.21	3.21
	2.0	0.5	2.36	2.37
	3.0	0.5	1.33	1.35
	4.0	0.5	4.61×10^{-1}	5.41×10^{-1}

Table 4.1 Comparison of numerical and analytic results for test case 1

4.2 One-Dimensional Radial Diffusion with a Constant Concentration Source Term

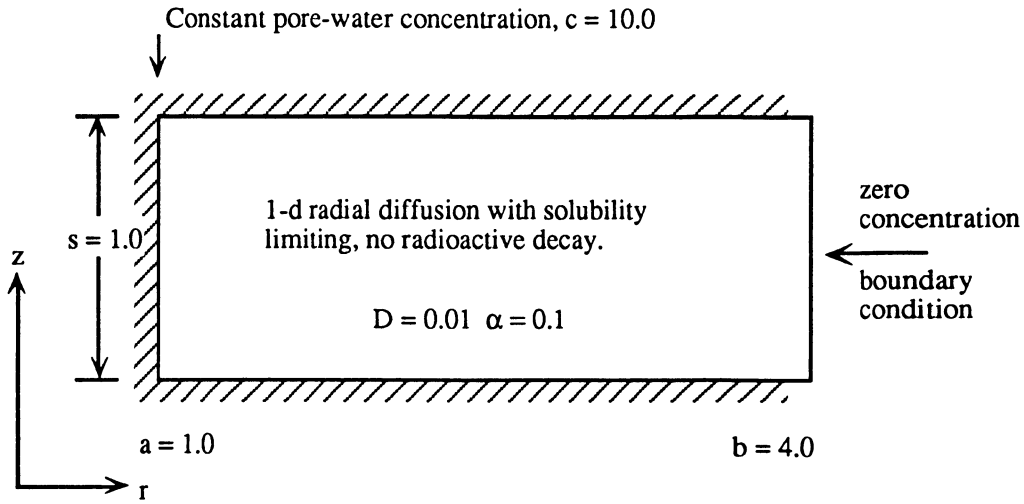

Figure 4.2 Schematic Representation of Test Case 2

The physical system is illustrated in figure 4.2. The positions of the radial boundaries are changed and there is now a source of constant concentration at the inner boundary. In the numerical model this boundary condition is modelled as a solubility limited source term with solubility 10 mass units per unit volume. The region is discretized into 10 columns with increments of 0.2 and 0.3 and 4 rows, with the same increments as in case 1. The time-step is unchanged.

The results are presented in table 4.2. Comparison of the analytic and numerical model results indicate that the accuracy of the numerical model is reduced where steep concentration gradients exist, as in this example. At early times the zero concentration boundary condition appears to enhance the diffusion. At later times, when the system reaches equilibrium, it results in lower concentrations throughout the mesh, compared with the analytical model results. Percentage errors range from 1.5% at radius 1.5 to 15% at radius 3.0.

Time	Radial Coordinate	Vertical Coordinate	Concentration	
			(Numerical)	(Analytic)
1.0	1.5	0.7	2.16	2.17
	2.0		2.37×10^{-1}	1.81×10^{-1}
	2.5		1.32×10^{-2}	5.08×10^{-3}
	3.0		5.49×10^{-4}	4.49×10^{-5}
2.0	1.5	0.7	3.55	3.55
	2.0		8.5×10^{-1}	8.17×10^{-1}
	2.5		1.34×10^{-1}	1.14×10^{-1}
	3.0		1.55×10^{-2}	9.16×10^{-3}
5.0	1.5	0.7	5.14	5.14
	2.0		2.31	2.30
	2.5		8.79×10^{-1}	8.68×10^{-1}
	3.0		2.79×10^{-2}	2.69×10^{-1}
10.0	1.5	0.7	6.06	6.06
	2.0		3.51	3.51
	2.5		1.88	1.89
	3.0		8.82×10^{-1}	9.17×10^{-1}
20.0	1.5	0.7	6.70	6.73
	2.0		4.42	4.49
	2.5		2.76	2.87
	3.0		1.50	1.66
100.0	1.5	0.7	6.97	7.08
	2.0		4.81	5.00
	2.5		3.14	3.39
	3.0		1.77	2.08

Table 4.2 Comparison of numerical and analytic results for test case 2

4.3 Two-Dimensional Diffusion with a Delta-Function, Z-Dependant Source Term

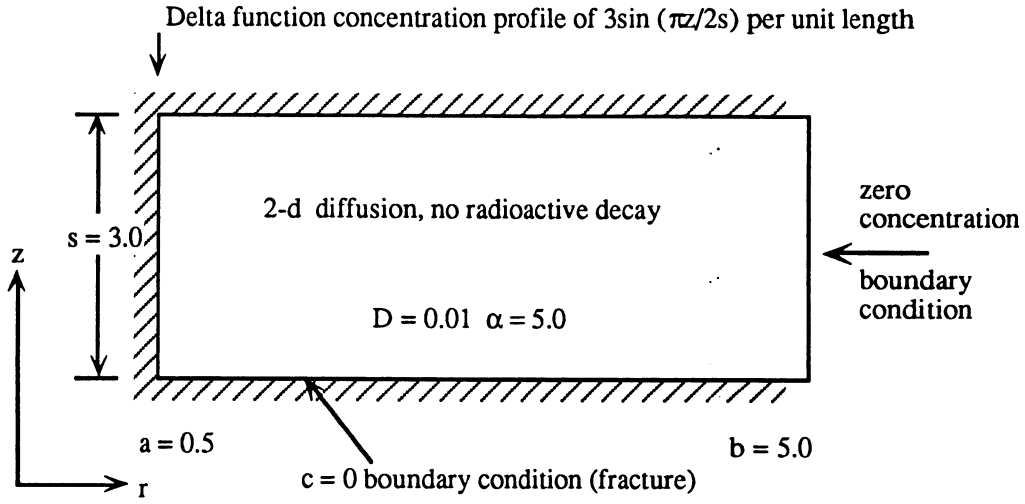

Figure 4.3 Schematic Representation of Test Case 3

The physical system is illustrated in figure 4.3. The capacity factor is increased from 0.1 to 5.0 and the lower boundary condition is one of zero concentration. The source has a profile of strength $3\sin(\pi z/2s)$ per unit length. In the numerical model, each source cell is assigned an initial concentration of $3\sin(\pi z/2s).\delta z/V$, where z denotes the z coordinate of a cell node, δz is the cell height, s is the cylinder height and V is the cell volume. The region is discretized into 22 columns of cell width 0.2 length units and 15 rows, each also of width 0.2 units, with a time-step of 10 units. The results are presented in table 4.3. Good agreement is obtained at later times, although the concentrations in the cells close to the far boundary are up to 9% below the analytic model values. The results at early times are in error by as much as 50%. The boundary condition clearly has a strong influence on the transient behaviour of the system, particularly for strongly sorbed species. Comparison is also made in this case of the flux into the fracture, represented by the zero concentration condition along the $z = 0$ boundary. Excellent agreement of within 1% of the analytic results is obtained, as shown in table 4.4.

Time	Radial Coordinate	Vertical Coordinate	Concentration	
			(Numerical)	(Analytic)
50.0	1.0	1.0	5.01×10^{-2}	5.01×10^{-2}
		2.0	8.67×10^{-2}	8.84×10^{-2}
	2.0	1.0	4.55×10^{-4}	2.73×10^{-4}
		2.0	7.88×10^{-4}	4.73×10^{-4}
	3.0	1.0	5.22×10^{-7}	1.04×10^{-8}
		2.0	9.04×10^{-7}	1.80×10^{-8}
100.0	1.0	1.0	4.25×10^{-2}	4.27×10^{-2}
		2.0	7.33×10^{-2}	7.39×10^{-2}
	2.0	1.0	3.04×10^{-3}	2.91×10^{-3}
		2.0	5.25×10^{-3}	5.04×10^{-3}
	3.0	1.0	3.18×10^{-5}	1.69×10^{-5}
		2.0	5.50×10^{-5}	2.93×10^{-5}
	4.0	1.0	9.68×10^{-8}	8.31×10^{-9}
		2.0	1.68×10^{-7}	1.44×10^{-8}
200.0	1.0	1.0	2.88×10^{-2}	2.86×10^{-2}
		2.0	4.93×10^{-2}	4.95×10^{-2}
	2.0	1.0	7.12×10^{-3}	7.13×10^{-3}
		2.0	1.23×10^{-2}	1.24×10^{-2}
	3.0	1.0	5.54×10^{-4}	5.20×10^{-4}
		2.0	9.37×10^{-4}	9.00×10^{-4}
	4.0	1.0	1.54×10^{-5}	1.11×10^{-5}
		2.0	2.67×10^{-5}	1.92×10^{-5}
500.0	1.0	1.0	1.30×10^{-2}	1.29×10^{-2}
		2.0	2.23×10^{-2}	2.23×10^{-2}
	2.0	1.0	7.20×10^{-3}	7.18×10^{-3}
		2.0	1.24×10^{-2}	1.24×10^{-2}
	3.0	1.0	2.44×10^{-3}	2.44×10^{-3}
		2.0	4.22×10^{-3}	4.22×10^{-3}
	4.0	1.0	4.94×10^{-4}	5.00×10^{-4}
		2.0	8.55×10^{-4}	8.67×10^{-4}

Table 4.3 Comparison of numerical and analytic results for test case 3

Time	Flux into Fracture	
	Numerical	Analytic
50.0	3.05×10^{-3}	3.06×10^{-3}
100.0	3.00×10^{-3}	2.97×10^{-3}
200.0	2.83×10^{-3}	2.81×10^{-3}
500.0	2.37×10^{-3}	2.37×10^{-3}

Table 4.4 Comparison of the flux from the numerical and analytic models for test case 3

4.4 Two-Dimensional Diffusion with Constant Concentration Source Term

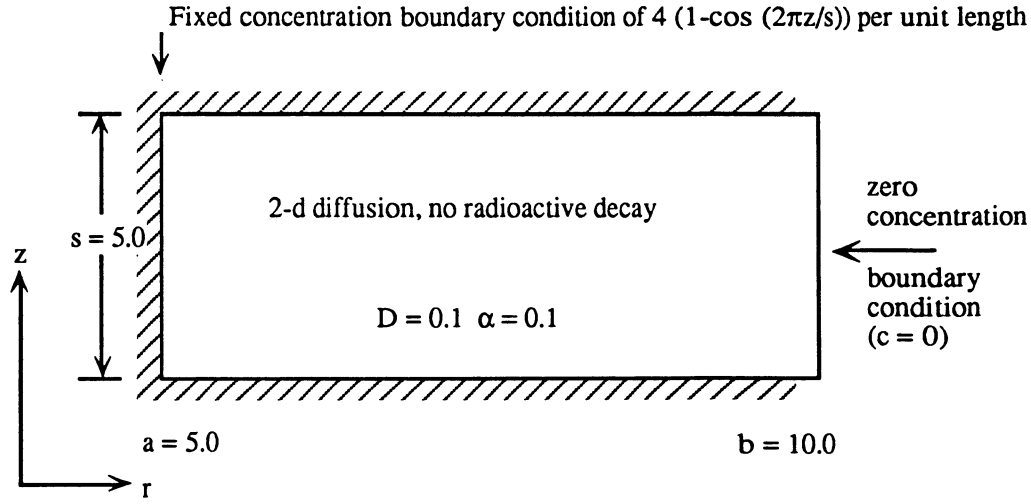

Figure 4.4 Schematic Representation of Test Case 4

This case is illustrated in figure 4.4. The inner and outer radial boundaries are at 5.0 and 10.0 arbitrary units respectively and the cylinder hieght is 5.0 units. The concentration at the inner boundary is constant, with a z-dependent profile of 4(1-cos($2\pi z/s$)) per unit length. In the numerical scheme this is achieved by reassigning the concentration in the source cells at the start of each new time-step. The region is discretized into 20 columns of widths 0.2 and 0.3 units, 21 rows of width 0.25 units, with a time-step of 0.02 units. A selection of results at various times is given in table 4.5. The accuracy of the numerical model results are reduced by the approximation to the surface source, in addition to the errors introduced by the space and time discretizations. Percentage errors of up to 20% occur at early times, improving to under 10% as the system approaches dynamic equilibrium.

Time	Radial Coordinate	Vertical Coordinate	Concentration	
			(Numerical)	(Analytic)
1.0	6.0	0.0	6.66×10^{-1}	7.79×10^{-1}
		1.0	1.53	1.45
		2.5	2.99	2.73
	7.0	0.0	3.10×10^{-1}	3.28×10^{-1}
		1.0	5.08×10^{-1}	4.70×10^{-1}
		2.5	8.31×10^{-1}	7.40×10^{-1}
	8.0	0.0	7.55×10^{-2}	7.42×10^{-2}
		1.0	1.10×10^{-1}	9.73×10^{-2}
		2.5	1.66×10^{-1}	1.41×10^{-1}
2.0	6.0	0.0	1.06	1.23
		1.0	1.98	1.94
		2.5	3.52	3.30
	7.0	0.0	7.62×10^{-1}	8.13×10^{-1}
		1.0	1.02	9.97×10^{-1}
		2.5	1.44	1.35×10^{-1}
	8.0	0.0	3.48×10^{-1}	3.58×10^{-1}
		1.0	4.15×10^{-1}	4.04×10^{-1}
		2.5	5.24×10^{-1}	4.90×10^{-1}
10.0	6.0	1.0	2.52	2.6
		2.5	4.07	3.96
	7.0	1.0	1.82	1.93
		2.5	2.25	2.29
	8.0	1.0	1.09	1.23
		2.5	1.21	1.32
20.0	6.0	1.0	2.53	2.63
		2.5	4.08	3.99
	7.0	1.0	1.84	1.97
		2.5	2.27	2.33
	8.0	1.0	1.11	1.26
		2.5	1.23	1.36

Table 4.5 Comparison of numerical and analytic results for test case 4

4.5 One-Dimensional Radial Diffusion with a 3-Nuclide Decay Chain

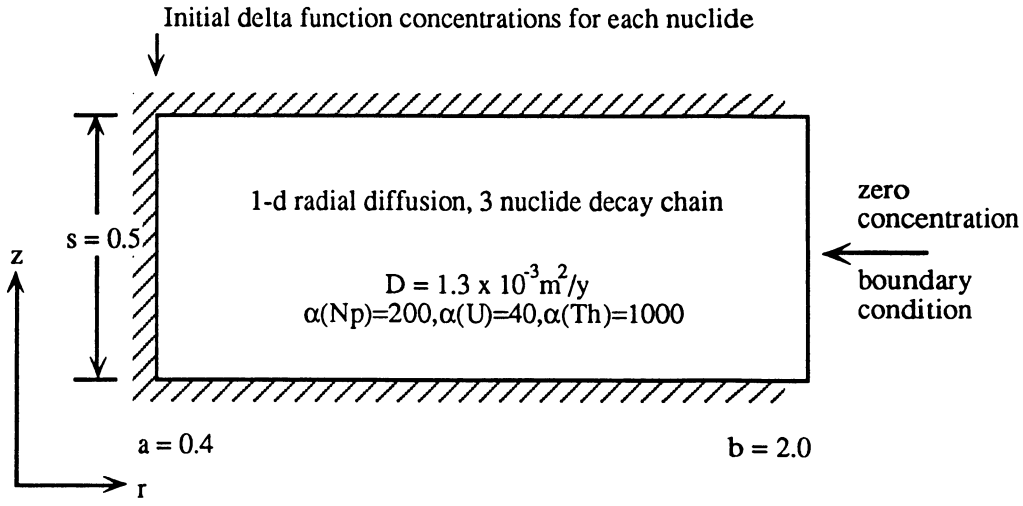

Figure 4.5 Schematic Representation of Test Case 5

This case is illustrated in figure 4.5. The inventory, diffusion coefficient and capacity factors are taken from reference [9]. A 3-nuclide chain (Np-237, U-233, Th-229) with corresponding inventories of 2.44, 4.67 $\times 10^{-4}$ and 0.0 GBq is used. The inventory figures are scaled down by a factor of 9, the ratio of the waste cylinder height (4.5 m) to the half-spacing between fractures (0.5 m), the latter being the section of the near-field system modelled by the CALIBRE code. The cylinder material is assigned the properties of bentonite, under reducing conditions. Solubility limits are set artificially high, so that precipitation does not occur. Zero flux boundary conditions are imposed at the upper and lower surfaces of the region, with a zero concentration far boundary condition. In the analytic model, the source is introduced as a linearly distributed surface delta-function at the inner radial boundary. In the numerical model, the inventory in each of the source cells is specified so that their total concentrations are equal. The region is discretized into 10 columns of widths 0.1, 0.15 and 0.2m and 5 rows of depth 0.1m, and a time-step of 200 years is used.

The results are given in tables 4.6-4.8. Agreement between the analytic and numerical models is generally good (within 5%) with the exception of Np-237 at 10^4 years and radius 1.6m.

Time (y)	Radial Coord. (m)	Vertical Coord. (m)	Np-237 Conc. (moles/m^3)	
			(Numerical)	(Analytic)
1×10^4	0.8	0.25	1.05×10^{-3}	1.08×10^{-3}
	1.2	0.25	1.52×10^{-4}	1.50×10^{-4}
	1.6	0.25	1.01×10^{-5}	6.22×10^{-6}
2×10^4	0.8	0.25	9.12×10^{-4}	9.17×10^{-4}
	1.2	0.25	3.22×10^{-4}	3.31×10^{-4}
	1.6	0.25	6.55×10^{-5}	6.46×10^{-5}
5×10^4	0.8	0.25	5.54×10^{-4}	5.54×10^{-4}
	1.2	0.25	3.50×10^{-4}	3.53×10^{-4}
	1.6	0.25	1.53×10^{-4}	1.56×10^{-4}
1×10^5	0.8	0.25	3.03×10^{-4}	3.02×10^{-4}
	1.2	0.25	2.16×10^{-4}	2.16×10^{-4}
	1.6	0.25	1.07×10^{-4}	1.08×10^{-4}
2×10^5	0.8	0.25	1.00×10^{-4}	9.95×10^{-5}
	1.2	0.25	7.23×10^{-5}	7.17×10^{-5}
	1.6	0.25	3.63×10^{-5}	3.60×10^{-5}
5×10^5	0.8	0.25	3.69×10^{-6}	3.57×10^{-6}
	1.2	0.25	2.66×10^{-6}	2.58×10^{-6}
	1.6	0.25	1.33×10^{-6}	1.29×10^{-6}

Table 4.6 Comparison of numerical and analytic results for test case 5, Np-237

Time (y)	Radial Coord. (m)	Vertical Coord. (m)	U-233 Conc. (moles/m^3)	
			(Numerical)	(Analytic)
1×10^4	0.8	0.25	1.25×10^{-5}	1.26×10^{-5}
	1.2	0.25	5.35×10^{-6}	5.45×10^{-6}
	1.6	0.25	1.65×10^{-6}	1.67×10^{-6}
2×10^4	0.8	0.25	1.66×10^{-5}	1.66×10^{-5}
	1.2	0.25	9.86×10^{-6}	9.96×10^{-6}
	1.6	0.25	4.13×10^{-6}	4.19×10^{-6}
5×10^4	0.8	0.25	1.66×10^{-5}	1.65×10^{-5}
	1.2	0.25	1.16×10^{-5}	1.16×10^{-5}
	1.6	0.25	5.68×10^{-5}	5.70×10^{-5}
1×10^5	0.8	0.25	1.04×10^{-5}	1.03×10^{-5}
	1.2	0.25	7.45×10^{-6}	7.40×10^{-6}
	1.6	0.25	3.73×10^{-6}	3.71×10^{-6}
2×10^5	0.8	0.25	3.47×10^{-6}	3.42×10^{-6}
	1.2	0.25	2.50×10^{-6}	2.46×10^{-6}
	1.6	0.25	1.25×10^{-6}	1.24×10^{-6}
5×10^5	0.8	0.25	1.28×10^{-7}	1.23×10^{-7}
	1.2	0.25	9.21×10^{-8}	8.86×10^{-8}
	1.6	0.25	4.23×10^{-8}	4.45×10^{-8}

Table 4.7 Comparison of numerical and analytic results for test case 5, U-233

Time (y)	Radial Coord. (m)	Vertical Coord. (m)	Th-229 Conc. (moles/m^3)	
			(Numerical)	(Analytic)
1×10^4	0.8	0.25	9.16×10^{-9}	9.28×10^{-9}
	1.2	0.25	3.01×10^{-9}	3.06×10^{-9}
	1.6	0.25	7.53×10^{-10}	7.50×10^{-10}
2×10^4	0.8	0.25	2.04×10^{-8}	2.05×10^{-8}
	1.2	0.25	1.06×10^{-8}	1.07×10^{-8}
	1.6	0.25	3.97×10^{-9}	4.02×10^{-9}
5×10^4	0.8	0.25	3.04×10^{-8}	3.03×10^{-8}
	1.2	0.25	2.08×10^{-8}	2.08×10^{-8}
	1.6	0.25	9.95×10^{-9}	10.0×10^{-8}
1×10^5	0.8	0.25	2.09×10^{-8}	2.07×10^{-8}
	1.2	0.25	1.50×10^{-8}	1.49×10^{-8}
	1.6	0.25	7.51×10^{-9}	7.46×10^{-9}
2×10^5	0.8	0.25	7.07×10^{-9}	6.97×10^{-9}
	1.2	0.25	5.10×10^{-9}	5.03×10^{-9}
	1.6	0.25	2.56×10^{-9}	2.52×10^{-9}
5×10^5	0.8	0.25	2.60×10^{-10}	2.50×10^{-10}
	1.2	0.25	1.88×10^{-10}	1.81×10^{-10}
	1.6	0.25	9.43×10^{-11}	9.07×10^{-11}

Table 4.8 Comparison of numerical and analytic results for test case 5, Th-229

4.6 Two-Dimensional Diffusion with a 3-Nuclide Decay Chain

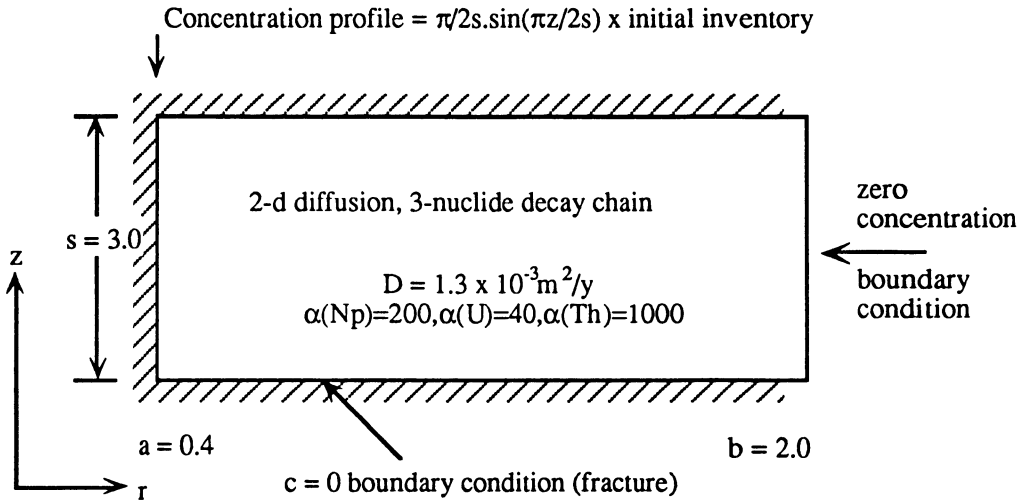

Figure 4.6 Schematic Representation of Test Case 6

The final case is illustrated in figure 4.6. The same nuclides and physical parameters as in the previous case are used, but the lower boundary condition is changed to one of zero concentration (equivalent to high advective flow in a fracture) and the concentration profile along the inner radial boundary is set to the initial inventory of each nuclide, weighted by the factor $\pi sin(\pi z/2s)/2s$. The same radial discretization is used, but the discretization in the vertical direction is increased to 6 rows. The time-step is again fixed at 200 years.

The results for the two models are shown in tables 4.9-4.11. Overall the agreement is very good, again with the exception of the result for Np-237 at 10^4 years and radius 1.6. Comparison is also made for the flux into the fracture, tables 4.12-4.13. The agreement is better than 13% over all nuclides, with increasing concurrence at later times.

Time (y)	Radial Coord. (m)	Vertical Coord. (m)	Np-237 Conc. (moles/m^3)	
			(Numerical)	(Analytic)
1×10^4	0.8	0.45	8.62×10^{-4}	8.79×10^{-4}
		0.25	6.17×10^{-4}	6.29×10^{-4}
	1.2	0.45	1.25×10^{-4}	1.23×10^{-4}
		0.25	8.92×10^{-5}	8.78×10^{-5}
	1.6	0.45	8.34×10^{-6}	5.08×10^{-6}
		0.25	5.96×10^{-6}	3.64×10^{-6}
2×10^4	0.8	0.45	3.98×10^{-4}	3.94×10^{-4}
		0.25	2.85×10^{-4}	2.82×10^{-4}
	1.2	0.45	1.40×10^{-4}	1.42×10^{-4}
		0.25	1.00×10^{-4}	1.02×10^{-4}
	1.6	0.45	2.85×10^{-5}	2.78×10^{-5}
		0.25	2.04×10^{-5}	1.99×10^{-5}
5×10^4	0.8	0.45	3.59×10^{-5}	3.47×10^{-5}
		0.25	2.57×10^{-5}	2.49×10^{-5}
	1.2	0.45	2.26×10^{-5}	2.21×10^{-5}
		0.25	1.62×10^{-5}	1.59×10^{-5}
	1.6	0.45	9.85×10^{-6}	9.77×10^{-6}
		0.25	7.04×10^{-6}	6.99×10^{-6}
1×10^5	0.8	0.45	8.15×10^{-7}	7.67×10^{-7}
		0.25	5.83×10^{-7}	5.49×10^{-7}
	1.2	0.45	5.79×10^{-7}	5.49×10^{-7}
		0.25	4.14×10^{-7}	3.93×10^{-7}
	1.6	0.45	2.87×10^{-7}	2.73×10^{-7}
		0.25	2.05×10^{-7}	1.96×10^{-7}

Table 4.9 Comparison of numerical and analytic results for test case 6, Np-237

Time (y)	Radial Coord. (m)	Vertical Coord. (m)	U-233 Conc. ($moles/m^3$) (Numerical)	U-233 Conc. ($moles/m^3$) (Analytic)
1×10^4	0.8	0.45	4.29×10^{-6}	4.22×10^{-6}
		0.25	3.07×10^{-6}	3.02×10^{-6}
	1.2	0.45	1.44×10^{-6}	1.44×10^{-6}
		0.25	1.03×10^{-6}	1.03×10^{-6}
	1.6	0.45	3.43×10^{-7}	3.32×10^{-7}
		0.25	2.45×10^{-7}	2.37×10^{-7}
2×10^4	0.8	0.45	1.99×10^{-6}	1.93×10^{-6}
		0.25	1.43×10^{-6}	1.38×10^{-6}
	1.2	0.45	9.65×10^{-7}	9.57×10^{-7}
		0.25	6.90×10^{-7}	6.85×10^{-7}
	1.6	0.45	3.18×10^{-7}	3.16×10^{-7}
		0.25	2.27×10^{-7}	2.26×10^{-7}
5×10^4	0.8	0.45	1.90×10^{-7}	1.81×10^{-7}
		0.25	1.36×10^{-7}	1.30×10^{-7}
	1.2	0.45	1.26×10^{-7}	1.22×10^{-7}
		0.25	8.99×10^{-8}	8.70×10^{-8}
	1.6	0.45	5.81×10^{-8}	5.67×10^{-8}
		0.25	4.15×10^{-8}	4.06×10^{-8}
1×10^5	0.8	0.45	4.40×10^{-9}	4.08×10^{-9}
		0.25	3.15×10^{-9}	2.92×10^{-9}
	1.2	0.45	3.13×10^{-9}	2.93×10^{-9}
		0.25	2.24×10^{-9}	2.10×10^{-9}
	1.6	0.45	1.56×10^{-9}	1.46×10^{-9}
		0.25	1.11×10^{-9}	1.05×10^{-9}

Table 4.10 Comparison of numerical and analytic results for test case 6, U-233

Time (y)	Radial Coord. (m)	Vertical Coord. (m)	Th-229 Conc. (moles/m^3)	
			(Numerical)	(Analytic)
1×10^4	0.8	0.45	4.66×10^{-9}	4.66×10^{-9}
		0.25	3.34×10^{-9}	3.34×10^{-9}
	1.2	0.45	1.15×10^{-9}	1.14×10^{-9}
		0.25	8.19×10^{-10}	8.13×10^{-10}
	1.6	0.45	2.17×10^{-10}	2.04×10^{-10}
		0.25	1.55×10^{-10}	1.46×10^{-10}
2×10^4	0.8	0.45	4.54×10^{-9}	4.48×10^{-9}
		0.25	3.29×10^{-9}	3.21×10^{-9}
	1.2	0.45	1.74×10^{-9}	1.73×10^{-9}
		0.25	1.24×10^{-9}	1.24×10^{-9}
	1.6	0.45	4.76×10^{-10}	4.67×10^{-10}
		0.25	3.41×10^{-10}	3.34×10^{-10}
5×10^4	0.8	0.45	8.03×10^{-10}	7.71×10^{-10}
		0.25	5.75×10^{-10}	5.52×10^{-10}
	1.2	0.45	4.71×10^{-10}	4.60×10^{-10}
		0.25	3.37×10^{-10}	3.30×10^{-10}
	1.6	0.45	1.95×10^{-10}	1.93×10^{-10}
		0.25	1.40×10^{-10}	1.38×10^{-10}
1×10^5	0.8	0.45	2.16×10^{-11}	2.03×10^{-11}
		0.25	1.55×10^{-11}	1.45×10^{-11}
	1.2	0.45	1.50×10^{-11}	1.42×10^{-11}
		0.25	1.07×10^{-11}	1.02×10^{-11}
	1.6	0.45	7.30×10^{-12}	6.96×10^{-12}
		0.25	5.22×10^{-12}	4.98×10^{-12}

Table 4.11 Comparison of numerical and analytic results for test case 6, Th-229

Time (y)	Flux into fracture, (moles/y)			
	Np-237		U-233	
	Numerical	Analytic	Numerical	Analytic
1×10^4	1.16×10^{-5}	1.33×10^{-5}	7.20×10^{-8}	7.48×10^{-8}
2×10^4	6.37×10^{-6}	6.94×10^{-6}	3.89×10^{-8}	3.98×10^{-8}
5×10^4	8.09×10^{-7}	8.42×10^{-7}	4.46×10^{-9}	4.56×10^{-9}
1×10^5	2.02×10^{-8}	2.03×10^{-8}	1.12×10^{-10}	1.08×10^{-10}
2×10^5	1.16×10^{-11}	1.10×10^{-11}	6.39×10^{-11}	5.86×10^{-11}

Table 4.12 Comparison of flux for test case 6, Np-237 and U-233

Time (y)	Flux into fracture, (moles/y) Th-229	
	Numerical	Analytic
1×10^4	6.98×10^{-11}	7.87×10^{-11}
2×10^4	7.73×10^{-11}	8.36×10^{-11}
5×10^4	1.72×10^{-11}	1.79×10^{-11}
1×10^5	5.25×10^{-13}	5.29×10^{-13}
2×10^5	3.13×10^{-16}	2.98×10^{-16}

Table 4.13 Comparison of flux test case 6, Th-229

4.7 Conclusions

Overall the agreement between the analytic and numerical models is very good, verifying the correct behaviour of the numerical model for the cases considered above. The cases also illustrate the importance of choosing a sufficiently fine mesh discretization, to achieve accurate results. Shorter time-steps are also required during the transient phases when steep concentration gradients may occur and when modelling nuclides with relatively short half-lives. Special care is also needed in choosing the position of the far boundary, to ensure it does not significantly influence the results.

4.8 Verification of the Radial Flow Approximation

A number of test cases were also performed to verify the radial flow approximation employed in CALIBRE. In the KBS-3 report [8] the flow of nuclide i from the nearfield is calculated as a rate N_i defined by the equation

$$N_i = Q_{eq}.C_{oi}. \tag{58}$$

C_{oi} is the concentration of nuclides in the fuel pore-water and Q_{eq} is the equivalent water flow that arrives at the canister with zero concentration of nuclides and leaves it with a concentration of C_{oi}. If the nuclide is solubility limited at a concentration of $C_{i,sol}$ then the above equation becomes

$$N_i = Q_{eq}C_{i,sol}. \tag{59}$$

In the CALIBRE test cases a single long-lived nuclide is considered, with a sufficient source inventory for it to remain solubility limited in the canister pore-water throughout the simulations. To make the comparison with KBS-3, the effective diffusivity of the rock is set to a very low value to inhibit matrix diffusion. The flow velocity of the water through a fracture of width 0.1mm is varied to determine the effect of the radial flow approximation at different flow rates. The simulations are run until the flux (F) leaving the system reaches an equilibrium value. From the calculated flux and elemental solubility limit under reducing conditions values of Q_{eq} are calculated for comparison with KBS-3:

$$Q_{eq} = \frac{F}{C_{i,sol}} \tag{60}$$

The results are listed in table 4.14. The $\pi cos\theta$ weighting function is used. Results obtained using the alternative weighting funtion of 2 are not significantly different. At low Darcy velocities, the Q_{eq} values calculated using CALIBRE agree reasonably well with the KBS-3 values [8]. At higher flows, the radial flow approximation predicts a higher flux than KBS-3.

Water Flow Velocity $l/m^2/y$	CALIBRE Q_{eq} $l/canister/y$	KBS-3 Q_{eq} $l/canister/y$
0.1	0.65	0.57
0.3	0.9	0.94
1.0	1.8	1.57
3.0	3.8	2.41

Table 4.14 Comparison of KBS-3 and CALIBRE Q_{eq} Values

The buffer, rock matrix and fracture water provide a diffusive barrier to the radionuclides. If there is no sorption, then diffusive transit times depend on the effective diffusion coefficients of each component. Transit times may be estimated simply by examination of the analytic solutions to the one-dimensional diffusion equation for a contaminant source of constant concentration, diffusing into a semi-infinite medium. The solution takes the form of an error function in which distances are scaled by the quantity $\sqrt{Dt}$, where D is the diffusivity and t is the time. For a distance of approximately 0.4m (buffer width) the diffusion time which matches this diffusion distance is of the order of 100 years. This will apply directly for a non-sorbed nuclide and will otherwise be multiplied by the retardation.

The delay arising from diffusion will be enhanced by the rock matrix and fracture. If the rock matrix diffusion is neglected, the delay in the release of a long-lived radionuclide to the far-field when there is virtually no sorption in the bentonite or fracture is shown in figure 4.7. Release from the canister occurs at 10^4 years, where the nuclide is kept at a constant concentration equal to its solubility limit. The flow rate is 0.1 $l/m^2/y$. The flux is transformed to an equivalent flow factor by normalisation with the elemental solubility limit. It can be seen that with no sorption in the buffer a steady state flux is attained in the first few hundred years.

For nuclides which are sorbed in the buffer (with a distribution coefficient of the order of 0.1 m^3/kg) the steady state flux is attained by approximately 10^5 years, whilst for more strongly sorbed nuclides, the delay is of the order of 10^6 years. The effects of diffusion and sorption in the rock matrix on the above results are shown in figure 4.8. The steady-state flux is higher owing to flux escaping to the far field through the rock, as well as through the fracture. The KBS-3 Q-equivalent for this flux is 0.76. With virtually no sorption, the steady state flux is attained in approximately 3 x 10^4 years, compared with several hundred years for the case with no rock matrix diffusion. With an intermediate level of sorption, the flux is still only 10 per cent of the steady state flux after 2 x 10^5 years, whilst strongly sorbed nuclides are delayed for considerably longer. It is clear from these results that the primary factors in the retardation of nuclides released from the canister are diffusion and sorption in the rock matrix. In comparison, the delaying effects of diffusion and sorption in the buffer are at best only of second-order significance.

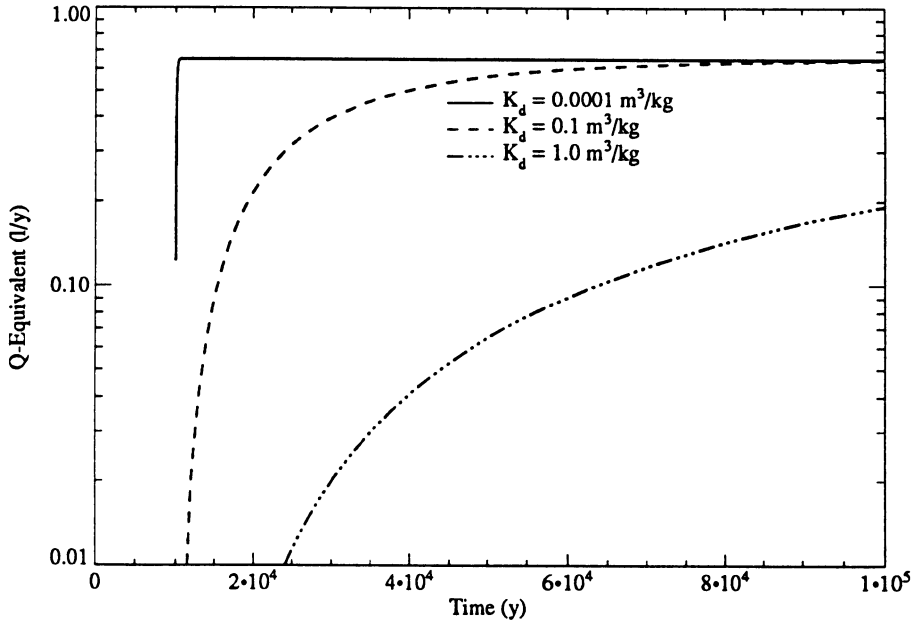

Figure 4.7 Equivalent Flow of the Near-Field with Sorption in the Buffer and no Matrix Diffusion

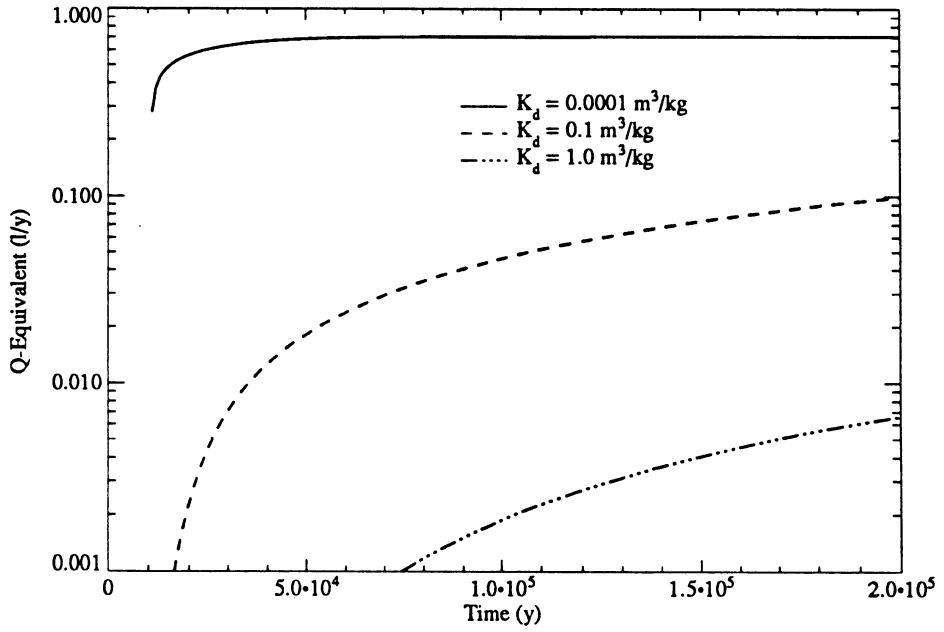

Figure 4.8 Equivalent Flow of the Near-Field with Matrix Diffusion and Sorption

References

[1] SKI Project-90 Summary Report, Vols. I, II, SKI TR 91:23, Swedish Nuclear Power Inspectorate, Stockholm, Sweden, August 1991.

[2] Shaw, W.T., The Motion of a Redox Front in a System of Bentonite and Rock, Incorporating Fracture Transport Effects, SKI TR 91:17, February 1992

[3] Shaw, W.T., The Oxidation State of the Near-field Environment in the CALIBRE Source Term Model: Further Remarks, SKI TR 91:20, March 1992.

[4] Hodgkinson, D.P., Robinson, P.C. & Pahwa, S.B., Preliminary Specifications of a Source Term Model for the Swedish Spent Fuel Disposal Concept, Intera Environmental Division Report I1794-1, Version 2, July 1988.

[5] Robinson, P.C., Verification Tests for Radionuclide Migration in CALIBRE, SKI TR 89:8, March 1989.

[6] Worgan, K., Robinson, P., Project-90 Near-Field Calculations Using CALIBRE, SKI TR 91:15, Swedish Nuclear Power Inspectorate, Stockholm, Sweden, 1992.

[7] Worgan, K., Robinson, P., CRYSTAL: A Model of a Fractured Rock Geosphere for Performance Assessment within Project-90, SKI TR 91:13, Swedish Nuclear Power Inspectorate, Stockholm, Sweden, 1992.

[8] SKBS/KBS, Final Storage of Spent Nuclear Fuel, KBS-3, 1983.

[9] Shaw, W., Smith, G., Worgan, K., Hodgkinson, D. and Andersson, K., Source Term Modelling Parameters for Project-90, SKI TR 91:27, Version 2, 1992.

www.ski.se

STATENS KÄRNKRAFTINSPEKTION
Swedish Nuclear Power Inspectorate

POST/POSTAL ADDRESS SE-106 58 Stockholm
BESÖK/OFFICE Klarabergsviadukten 90
TELEFON/TELEPHONE +46 (0)8 698 84 00
TELEFAX +46 (0)8 661 90 86
E-POST/E-MAIL ski@ski.se
WEBBPLATS/WEB SITE www.ski.se